

A discrete element and ray framework for rapid simulation of acoustical dispersion of microscale particulate agglomerations

T. I. Zohdi¹

Received: 19 September 2015 / Accepted: 21 December 2015
© Springer-Verlag Berlin Heidelberg 2016

Abstract In industry, particle-laden fluids, such as particle-functionalized inks, are constructed by adding fine-scale particles to a liquid solution, in order to achieve desired overall properties in both liquid and (cured) solid states. However, oftentimes undesirable particulate agglomerations arise due to some form of mutual-attraction stemming from near-field forces, stray electrostatic charges, process ionization and mechanical adhesion. For proper operation of industrial processes involving particle-laden fluids, it is important to carefully breakup and disperse these agglomerations. One approach is to target high-frequency acoustical pressure-pulses to breakup such agglomerations. The objective of this paper is to develop a computational model and corresponding solution algorithm to enable rapid simulation of the effect of acoustical pulses on an agglomeration composed of a collection of discrete particles. Because of the complex agglomeration microstructure, containing gaps and interfaces, this type of system is extremely difficult to mesh and simulate using continuum-based methods, such as the finite difference time domain or the finite element method. Accordingly, a computationally-amenable discrete element/discrete ray model is developed which captures the primary physical events in this process, such as the reflection and absorption of acoustical energy, and the induced forces on the particulate microstructure. The approach utilizes a staggered, iterative solution scheme to calculate the power transfer from the acoustical pulse to the particles and the subsequent changes (breakup) of the pulse due to the particles. Three-dimensional examples are provided to illustrate the approach.

Keywords Acoustics · Pulse · Particles

1 Introduction

In numerous industries, particle-laden fluids are a key part of the fabrication of products such as (1) casted machine parts, (2) additively manufactured and 3-D printed electronics and medical devices and even (3) slurry processed food, to name a few. Common to many of these areas are new types of solidified heterogeneous materials, comprised of particulates in a binding matrix. The macroscopic material characteristics of the material are dictated by the aggregate response of an assemblage of particles suspended in a binding matrix material. The fluid precursor to the final solid product is a particle-laden fluid, which are delivered through piping, nozzles and channels (Choi et al [15–17], Demko et al. [21,22] and Martin [48,49]).¹ Typically, such materials start in particulate form, and are then mixed with a binder and delivered as a flowing particle-laden fluid which is to be cast into their final shape.²

Often, in the mixing of these materials, agglomerations of particles occur, which need to be broken up and dispersed in order to ensure production of high-quality products (Figs. 1, 2). A unique feature of small-scale particulate systems is that they exhibit a strong sensitivity to inter-particle near-field forces, stemming from stray electrostatic

✉ T. I. Zohdi
zohdi@me.berkeley.edu

¹ Department of Mechanical Engineering, University of California, Berkeley, CA 94720-1740, USA

¹ Also, printed electronics, using processes such as high-resolution electrohydrodynamic-jet printing are also emerging as viable methods. For overviews, see Wei and Dong [62], who also develop specialized processes employing phase-change inks. Such processes are capable of producing micron-level footprints for high-resolution additive manufacturing.

² Over 50% of man-made materials start in granulated form (Duran [28] and Torquato [60]).

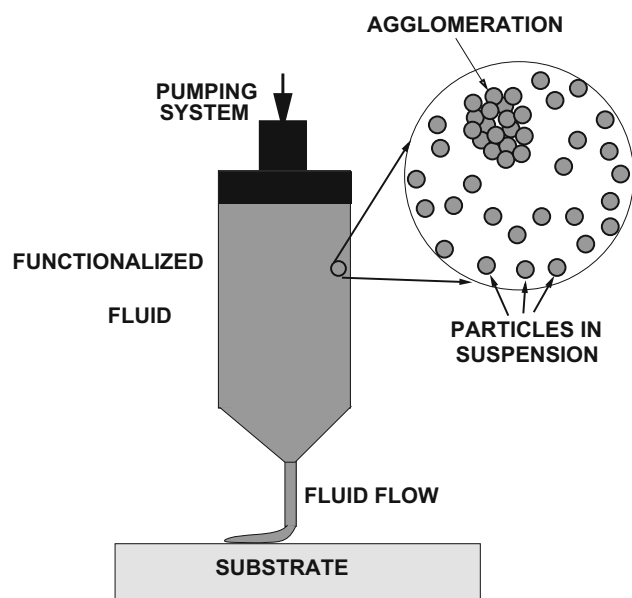


Fig. 1 A particle laden fluid in a channel with an agglomeration

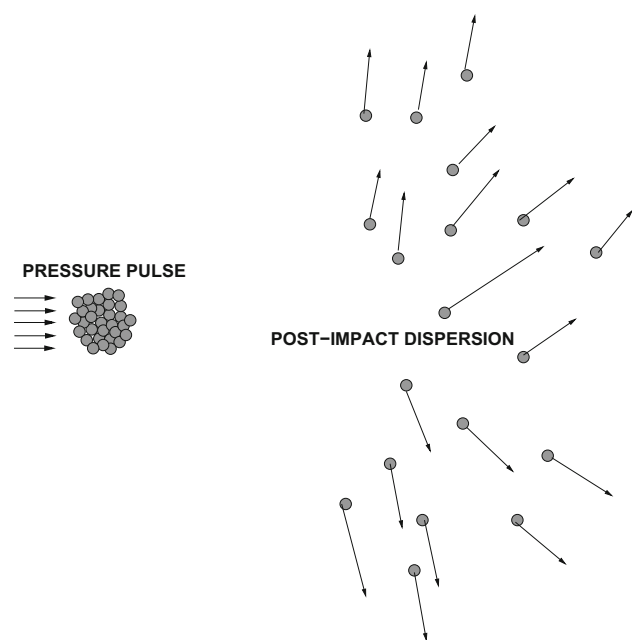


Fig. 2 Pulsing to break up and disperse an agglomeration

charges, process ionization and mechanical adhesion, leading to agglomeration and cluster formation, which can strongly affect manufactured product quality. These agglomerations can also remain coherent as suspended clusters in the fluid material during processing. Inadequate elimination of these clusters can lead to manufacturing inconsistencies/variability which can strongly affect the overall solidified product quality, in particular if the manufactured devices have small dimensions. Furthermore, in other cases, the agglomerations

can accumulate on the surfaces of manufacturing devices. For particle laden fluids delivered through channels, surface particulate agglomeration can lead to system malfunction, primarily due to clogging.

One approach to remove or break up the agglomerations is to acoustically pressure-pulse them (Fig. 2). Acoustical pulsing generally speaking, consists of an acoustical driver, which is a sound source that is powered by compressed air and an acoustical resonator which amplifies and guides the energy. Essentially, an acoustical pulser will produce a series of rapid pressure-peak pulses in a very targeted manner. Acoustical cleaning has been utilized in macroscale bulk processes, but its application on the microscale for precision manufacturing, as well as modeling and simulation, has been lacking. The key parameters are (a) the strength of the pulse and (b) the repetition of the the pulse.

A primary simulation issue is that the interaction of pressure pulses with the agglomeration leads to a set of coupled differential equations for the dynamics of the particles and the propagation and breakup of the pressure pulse. The objective of this paper is to develop a computational model and corresponding solution algorithm to enable rapid simulation of a pressure pulse's effect on an agglomeration, composed of aggregated discrete particles. Because of the complex agglomeration microstructure, containing gaps and interfaces, this type of system is extremely difficult to mesh and simulate the pressure pulse dynamics using continuum-based methods, such as the finite difference time domain method or the finite element method. Accordingly, a computationally-amenable discrete element/discrete ray model is developed which captures the primary physical events, such as the reflection and absorption of acoustical energy, and the forces induced onto the particulate microstructure, resulting in dynamics of large numbers of particles involving particle-to-particle contact. In the model, the agglomeration is represented by a discrete element method representation and the pressure pulse/shock wave is described by a collection of propagating rays with prescribed acoustical power content, direction and velocity. The approach also develops a staggered, iterative solution scheme, which is needed to calculate the power transfer from the acoustical pulse to the particles and the subsequent changes (breakup) of the pulse due to the particles. Three-dimensional examples are provided to illustrate the approach.

Remark 1 There is a variety of discrete element-like methods, for example see Onate et al. [51,52], Rojek et al. [55], Carbonell et al. [13], Labra and Onate [45], Leonardi et al. [46], Cante et al. [12], Rojek [56], Onate et al. [53], Bolintineanu et al. [9], Avci and Wriggers [5] and Zohdi [78–80]. In particular, we note the discrete element method has been used for particle agglomerations in acoustic fields, for instance in Markauskasa et al. [47]. The ray representation of waves can

be found in a variety of works, for example in Virovlyanskii [61], Borejko et al. [10] and Zohdi [73, 84–89] among others.

Remark 2 This work has direct applicability to the subject of “Design For Cleanability” which concerns itself with the advantageous manufacturing of devices, in particular those with interior keyways and channels, by assessing the ability to perform maintenance during the design phase. In many industrial systems, buildup of unwanted particulate material is inaccessible for removal, and ultimately leads to system malfunction. For more details, we refer the reader to Aurich and Dornfeld [4], Garg et al. [37], Avila et al. [6, 7]. Furthermore, residual particulate matter can also be present after a manufacturing process involving particles (see, for example, Luo and Dornfeld [41–44], Arbelaez et al. [2, 3], Ciampini et al. [18, 19], Gomes-Ferreira et al. [32], Ghobeity et al. [33, 34].³

Remark 3 We remark that in biological systems, oftentimes it is a goal to destroy certain types of agglomerations, such as kidney stones in shock wave lithotripsy (Zohdi [73]). The approach developed in this paper has direct applicability in this domain as well.

2 Dynamic response of an agglomeration

In order to represent the group of interacting particles, we follow a relatively flexible formulation found in Zohdi [80]. We consider a group of non-intersecting particles ($i = 1, 2, \dots, N_p$). The objects in the system are assumed to be small enough to be considered (idealized) as particles, spherical in shape, and that the effects of their rotation with respect to their mass center is unimportant to their overall motion, although, we will make further remarks on these effects shortly. The equation of motion for the i^{th} particle in system is

$$m_i \ddot{\mathbf{r}}_i = \Psi_i^{tot}(\mathbf{r}_1, \mathbf{r}_2, \dots, \mathbf{r}_{N_p}) = \Psi_{ii}^{ray} + \Psi_i^{con} + \Psi_i^{bond} + \Psi_i^{damp} + \Psi_i^{e+m}, \quad (1)$$

where \mathbf{r}_i is the position vector of the i th particle and where Ψ_i^{tot} represents all forces acting on particle i , which is decomposed into the sum of forces due to:

- Shock (transmitted ray) forces (Ψ_{ii}^{ray}),
- Inter-particle forces (Ψ_i^{con}) generated by contact with other particles,
- Adhesive bonding forces (Ψ_i^{bond}) with other particles,

³ Even techniques associated with shot peening can leave residual particulate matter. We also refer the reader to Afazov et al. [1], Bagherifard et al. [8], Elbella et al. [29], Chen et al. [14] and Zohdi [83].

- Damping forces arising from the surrounding interstitial environment (Ψ_i^{damp}) occurring from potentially viscous, surrounding, interstitial fluids, surfactants and
- External electromagnetic forces (Ψ_i^{e+m}) which can play a key role in small charged or magnetized particles.

In the next sections, we examine each of the types of forces in the system in detail.

3 Particle-shock wave contact

We consider cases where the wavelengths of incident high-frequency acoustical pressure waves (p-waves) are at least one order of magnitude smaller than the diameter (d) of the particle scatterers ($10^{-6} m \leq d \leq 10^{-4} m$). This length-scale ordering indicates that diffraction is minimal, and makes (geometric) ray-tracing techniques accurate.⁴ In such cases, geometric ray-tracing can be used to determine the amount of propagating incident energy that is reflected and the amount that is absorbed by multiple particles. For the benefit of readers unfamiliar with ray tracing, we remark that it is essentially an approximate solution to the wave equation, based on the Eikonal equation, which is the limiting case of wave phenomena as the wave length tends towards zero. Reviews of this classical topic are given in Appendix 1.

3.1 Ray tracing: incidence, reflection and transmission

The reflection of a ray at an interface is given by enforcing continuity of the (acoustical) pressure and disturbance velocity at that location; this yields the ratio between the incident and reflected pressures. We use a local coordinate system (Fig. 3), and enforce (1) that the number of waves per unit length in the x_1 -direction must be the same for the incident, reflected and refracted (transmitted) waves and (2) a pressure balance at the interface. After some algebra (see Appendix 1), this yields the reflectance for the (acoustical) power (energy per unit time)

$$\mathcal{R} = \frac{I_r}{I_i} = \left(\frac{\hat{A} \cos \theta_i - \cos \theta_t}{\hat{A} \cos \theta_i + \cos \theta_t} \right)^2, \quad (2)$$

where I_i is the incident (power) ray, I_r is the reflected (power) ray, I_t is the transmitted (power) ray, $\hat{A} \stackrel{\text{def}}{=} \frac{A_t}{A_i} \stackrel{\text{def}}{=} \frac{\rho_t c_t}{\rho_i c_i}$, ρ_t is the density of the medium which the ray encounters (transmitted), c_t is corresponding sound speed in that medium, A_t is the corresponding acoustical impedance, ρ_i is the density

⁴ Even if this wavelength to particle size ratio is not present, ray representation of p-waves is still often used, and can be considered as a way to approximately track the propagation of energy, however, without the ability to capture diffraction properly.

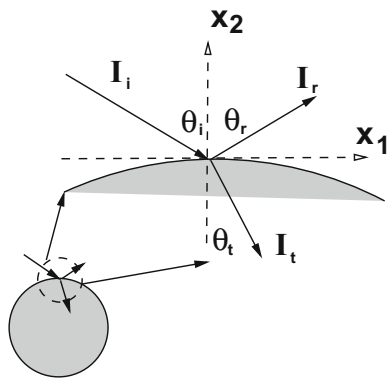


Fig. 3 Zoom on a ray-particle contact

of the medium in which the ray was traveling (incident), c_i is corresponding sound speed in that medium A_i is the corresponding acoustical impedance. The relationship (the law of refraction) between the incident and transmitted angles is $c_t \sin \theta_t = c_i \sin \theta_i$. Defining $\tilde{c} \stackrel{\text{def}}{=} \frac{c_i}{c_t}$, and studying asymptotic cases where $\sin \theta_t \rightarrow 1$, we have $\sin \theta_i \rightarrow \tilde{c}$, which identifies a so-called critical angle, where no energy is transmitted. A simple way of observing complete reflection is to set $\theta_t = \pi/2$ in

$$\mathcal{R} = \frac{I_r}{I_i} = \left(\frac{\hat{A} \cos \theta_i - \cos \theta_t}{\hat{A} \cos \theta_i + \cos \theta_t} \right)^2 = \left(\frac{\hat{A} \cos \theta_i - 0}{\hat{A} \cos \theta_i + 0} \right)^2 = 1. \tag{3}$$

Remark 1 A more rigorous way of analyzing the critical angle phenomena is to rewrite the reflection relation as $\mathcal{R} \stackrel{\text{def}}{=}} r \bar{r} = 1$, where \bar{r} is the complex conjugate, where $\mathcal{R} = r * \bar{r}$

$$r = \frac{\tilde{c} \hat{A} \cos \theta_i - j(\sin^2 \theta_i - \tilde{c}^2)^{\frac{1}{2}}}{\tilde{c} \hat{A} \cos \theta_i + j(\sin^2 \theta_i - \tilde{c}^2)^{\frac{1}{2}}}, \tag{4}$$

where $j = \sqrt{-1}$. For angles above the critical angle $\theta_i \geq \theta_i^*$, all of the energy is reflected. We note that when $A_t = A_i$ and $c_i = c_t$, then there is no reflection. Also, when $A_t \gg A_i$, then $r \rightarrow 1$, and when $A_t \ll A_i$, then $r \rightarrow -1$.

Remark 2 The power input (transmitted) from incidence and reflection is

$$I_t = I_i - I_r = I_i(1 - \mathcal{R}). \tag{5}$$

The overall force magnitude imparted by the ray can be determined by (see Appendix 1)

$$\begin{aligned} \text{power transmitted} &= \|\Psi_t^{ray}\| \|\mathbf{v}_t\| \\ &= \frac{\|\Psi_t^{ray}\| \|\Psi_t^{ray}\|}{\rho_t c_t a_r} = I_i(1 - \mathcal{R}), \end{aligned} \tag{6}$$

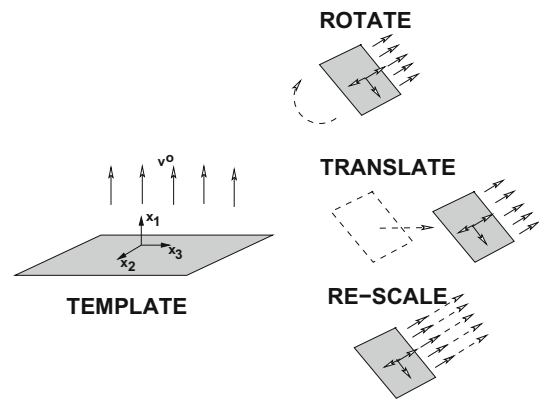


Fig. 4 Construction of the initial plane wave of rays

thus

$$\|\Psi_t^{ray}\| = \sqrt{I_i(1 - \mathcal{R})\rho_t c_t a_r}, \tag{7}$$

where the velocity in the transmitted medium is $\|\mathbf{v}_t\| = \frac{P_t}{\rho_t c_t}$, where P_t is the pressure content of the ray, and $\|\Psi_t^{ray}\| \propto \frac{P_t}{a_r}$, where a_r is a (pseudo) contact area parameter. The contact area parameter can be approximated from the total area of the original plane wave divided by the total number of rays. This is discussed further in the next section. The force's magnitude is projected in the direction of the transmitted ray, i.e. at the angle θ_t in the plane of incidence. This force is assumed to be completely absorbed by the particle and is not re-transmitted. The reflected ray is simply projected in the direction at the reflected angle, θ_r .

Remark 3 The initial plane wave of rays is generated by (Fig. 4):

- Generating a set of vectors in a ‘‘master template’’ domain,
- Rotating the master template to the desired direction of the pulse,
- Translating the rotated master template to the desired starting location.
- The vectors are then scaled according to the initial starting power content.

3.2 Acoustical-pulse computational algorithm

We now consider an initially coherent plane-wave composed of multiple (initially) parallel rays (Fig. 3). Each ray is a vector in the direction of the flow of energy, which, in isotropic media, corresponds to the normal to the wave front. For isotropic media, the rays are parallel to the wave propagation vector. It is of particular interest to describe the break-up of initially highly directional coherent beams which do not

spread out into multidirectional rays unless they encounter scatterers. It is convenient to define vectors for a ray by projecting the power onto the unit vector associated with the velocity

$$\mathbf{I} \stackrel{\text{def}}{=} I \frac{\mathbf{v}^{ray}}{\|\mathbf{v}^{ray}\|}, \tag{8}$$

where \mathbf{v}^{ray} is the velocity of the ray, $I = \|\mathbf{I}\|$ is the magnitude of the power and initially, $I_0 \stackrel{\text{def}}{=} \|\mathbf{I}(t = 0)\|$. To obtain the ray contributions from a beam, we simply partition the initial beam cross-section into equal rays, $Ia_r = Ia_b/N_r$, where N_r is the number of rays in the beam and where a_b is cross-sectional area of the beam. Later in the paper, we will elaborate more on the selection of the number of rays, which is determined by successive refinement of the number of rays in a pulse, until no appreciable differences occur. Clearly, I_0a_b can be considered the total power associated with the beam. The parameter a_r provides us with a way of appropriately distributing or ‘‘lumping’’ the amount of energy in the overall wave (beam) into rays. The computational algorithm is as follows, starting at $t = 0$ and ending at $t = T$, for an instantaneously fixed set of particles:

- | | |
|---|------------|
| <p>(1) Compute ray reflections (Fresnel Relation)</p> <p>(2) Compute energy absorbed by each particle :
 $\Delta I = (I_i - I_r) = (1 - \mathcal{R})I_i$</p> <p>(3) Compute induced forces each particle : Ψ_i^{ray}</p> <p>(4) Increment all ray positions :
 $\mathbf{r}_q^{ray}(t + \Delta t) = \mathbf{r}_q^{ray}(t) + \Delta t \mathbf{v}_q^{ray}(t), \quad q = 1, \dots, rays$</p> <p>(5) Go to (1) and repeat with $(t = t + \Delta t)$</p> | <p>(9)</p> |
|---|------------|

The time step size Δt is dictated by the size of the particles. A somewhat ad-hoc approach is to scale the time step size to be no larger than $\Delta t \propto \frac{\xi R}{\|\mathbf{v}^{ray}\|}$, where R is the nominal radius of the particles, $\|\mathbf{v}^{ray}\|$ is the magnitude of the velocity of the rays and ξ is a scaling factor, typically $0.05 \leq \xi \leq 0.1$. The required time step limitation is then also compared against other time step needed to integrate the particle dynamics properly, which we discuss next. This ensures that meaningful interactions are not skipped. *We now elaborate on the dynamics of the particles in Step (3) above.*

4 Particle-to-particle contact forces

Following Zohdi [80], we employ a simple particle overlap model to determine the normal contact force contributions from the surrounding particles (N_{ci}) in contact, $\Psi_i^{con,n} = \sum_{j=1}^{N_{ci}} \Psi_{ij}^{con,n}$, based on separation distance between particles in contact (Fig. 5). Generally,

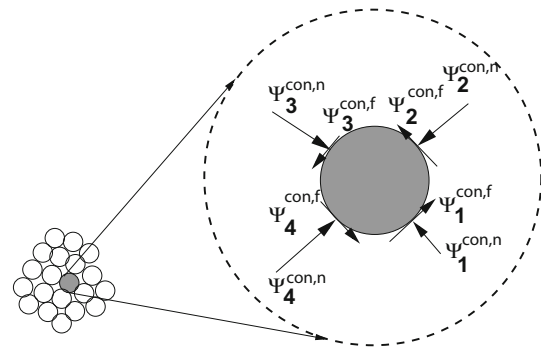


Fig. 5 Normal contact and friction forces induced by neighboring particles in contact (see Zohdi [80])

$$\Psi_{ij}^{con,n} = \mathcal{F}(\|\mathbf{r}_i - \mathbf{r}_j\|, R_i, R_j, \text{material parameters}). \tag{10}$$

There is no shortage of contact models, of varying complexity, to generate a contact interaction force. Throughout this work, we will utilize a particularly simple relation whereby contact force is proportional to the relative *normalized* proximity of particles i and j in contact, detected by the distance between centers being less that the sum of the radii

$$\text{If } \|\mathbf{r}_i - \mathbf{r}_j\| \leq R_i + R_j \Rightarrow \text{activate contact}, \tag{11}$$

where we define the overlap as

$$\delta_{ij} \stackrel{\text{def}}{=} \|\|\mathbf{r}_i - \mathbf{r}_j\| - (R_i + R_j)\|. \tag{12}$$

Accordingly, we consider the following

$$\Psi_{ij}^{con,c} \propto -K_{pij} |\mathcal{E}_{ij}|^{p_p} \mathbf{n}_{ij} A_{ij}^c, \tag{13}$$

where $0 < K_{pij} < \infty$ is a particle-to-particle contact compliance constant, p_p is a material parameter, \mathcal{E}_{ij} is normalized/nondimensional (strain-like) deformation metric

$$\mathcal{E}_{ij} = \left| \frac{\|\mathbf{r}_i - \mathbf{r}_j\| - (R_i + R_j)}{(R_i + R_j)} \right| = \frac{\delta_{ij}}{(R_i + R_j)} \tag{14}$$

and

$$\mathbf{n}_{ij} = -\frac{\mathbf{r}_i - \mathbf{r}_j}{\|\mathbf{r}_i - \mathbf{r}_j\|} = \frac{\mathbf{r}_j - \mathbf{r}_i}{\|\mathbf{r}_i - \mathbf{r}_j\|}, \tag{15}$$

where the R_i and R_j are the radii of particles i and j respectively. The term A_{ij}^c is a contact area parameter, which is discussed in Appendix 2. Appendix 2 also provides a brief review of alternative models, such as the classical Hertzian contact model.

4.1 Comments on rolling/spinning

The introduction of rolling and spin is questionable for a small object, idealized by a particle, in particular because of rolling resistance. In addition to the balance of linear momentum, $m_i \dot{\mathbf{v}}_i = \Psi_i^{tot}$, where the \mathbf{v}_i is the velocity of the center of mass, the equations of angular momentum read $\dot{\mathbf{H}}_{i,cm} = \frac{d(\bar{I}_i \cdot \boldsymbol{\omega}_i)}{dt} = \mathbf{M}_{i,cm}^{tot}$. For spheres, we have $\mathbf{H}_{i,cm} = \bar{I}_{i,s} \boldsymbol{\omega}_i = \frac{2}{5} m_i R_i^2 \boldsymbol{\omega}_i$ and for the time discretization

$$\boldsymbol{\omega}_i(t + \Delta t) = \boldsymbol{\omega}_i(t) + \frac{\Delta t}{\bar{I}_{i,s}} (\phi \mathbf{M}_{i,cm}^{tot}(t + \Delta t) + (1 - \phi) \mathbf{M}_{i,cm}^{tot}(t)), \tag{16}$$

where $\mathbf{M}_{i,cm}^{tot}$ are the total moments generated by interaction forces, such as contact forces and rolling resistance. For the applications at hand, the effects of rolling is generally negligible, in particular because the particles are small. However, nonetheless, we formulate the system with rotations where \mathbf{r}_i is the position of the center of mass, \mathbf{v}_i is the velocity of the center of mass and $\boldsymbol{\omega}_i$ is the angular velocity. An important quantity of interest is the velocity on the surface of the “particles”, which is a potential contact point with other particles, denoted \mathbf{v}_i^c

$$\mathbf{v}_i^c = \mathbf{v}_i + \boldsymbol{\omega}_i \times \mathbf{r}_{i \rightarrow c}, \tag{17}$$

where $\mathbf{r}_{i \rightarrow c}$ is the relative position vector from the center to the possible point of contact. This is utilized further later.

Remark We remark that had the transmitted moment from a ray been important, it would be computed via (Fig. 5)

$$\mathbf{M}_t^{ray} = (\mathbf{r}_c - \mathbf{r}_i) \times \Psi_t^{ray}, \tag{18}$$

where \mathbf{r}_c is the position of the contact point and \mathbf{r}_i is the center of the particle in question.

4.2 Contact dissipation

Phenomenological particle contact dissipation can be incorporated by tracking the relative velocity of the particles in contact. A simple model to account for this is

$$\Psi_{ij}^{con,d} = c^{cd} (\mathbf{v}_{j,n} - \mathbf{v}_{i,n}) A_{ij}^c, \tag{19}$$

where c^{cd} is a contact dissipation parameter.

4.3 Regularized contact friction models

Frictional stick is modelled via the following regularized friction algorithm: (at the point of contact)

- Check static friction threshold (K^f is a tangential contact friction compliance constant):

$$K^f \|\mathbf{v}_{j,\tau}^c - \mathbf{v}_{i,\tau}^c\| A_{ij}^c \Delta t \text{ against } \mu_s \|\Psi^{con,n}\|, \tag{20}$$

where $\|\mathbf{v}_{j,\tau}^c - \mathbf{v}_{i,\tau}^c\| \Delta t$ is the relative tangential velocity at a point of contact, Δt is the time-step used later in the numerical discretization⁵, μ_s is the static friction coefficient. *This step replaces (“regularizes”) a more rigorous, and difficult, step of first assuming no slip, generating the no-slip contact forces, by solving an entire multi-body/multisurface contact problem, Ψ^{ns} , and checking Ψ^{ns} against the threshold $\mu_s \|\Psi^{con,n}\|$ on each surface.*

- If the threshold is not met ($K^f \|\mathbf{v}_{j,\tau}^c - \mathbf{v}_{i,\tau}^c\| A_{ij}^c \Delta t < \mu_s \|\Psi^{con,n}\|$), then

$$\Psi^{con,f} = K^f \|\mathbf{v}_{j,\tau}^c - \mathbf{v}_{i,\tau}^c\| A_{ij}^c \Delta t \boldsymbol{\tau}_{ij}^c \tag{21}$$

where

$$\boldsymbol{\tau}_{ij}^c = -\frac{\mathbf{v}_{i,\tau}^c - \mathbf{v}_{j,\tau}^c}{\|\mathbf{v}_{j,\tau}^c - \mathbf{v}_{i,\tau}^c\|} = \frac{\mathbf{v}_{j,\tau}^c - \mathbf{v}_{i,\tau}^c}{\|\mathbf{v}_{j,\tau}^c - \mathbf{v}_{i,\tau}^c\|}, \tag{22}$$

where the subscripts indicate the tangential components of velocity. The tangential velocity at the contact point is obtained by subtracting away the normal component of the velocity

$$\mathbf{v}_i^c = \mathbf{v}^c - (\mathbf{v}^c \cdot \mathbf{n}) \mathbf{n}. \tag{23}$$

- If the threshold is met or exceeded ($K^f \|\mathbf{v}_{j,\tau}^c - \mathbf{v}_{i,\tau}^c\| A_{ij}^c \Delta t \geq \mu_s \|\Psi^{con,n}\|$), then one adopts a slip model of the form

$$\Psi_{ij}^{con,f} = \mu_d \|\Psi_{ij}^{con,n}\| \boldsymbol{\tau}_{ij}^c, \tag{24}$$

where μ_d is the dynamic friction coefficient.

4.4 Particle-to-particle bonding relation

For the particles to bond, we adopt a criterion based on exceeding a critical interpenetration distance. Explicitly:

- Recall, if $\|\mathbf{r}_i - \mathbf{r}_j\| \leq (R_i + R_j)$, then the particles are in contact and $\mathcal{E}_{ij} = \frac{\delta_{ij}}{(R_i + R_j)}$.
- If the particles are in contact and $|\mathcal{E}_{ij}| \geq \mathcal{E}^*$, then an (adhesive/attractive) normal bond is activated between the particles of the form

$$\Psi_{ij}^{bond,n} = K_{ij}^{nb} |\mathcal{E}_{ij}|^{pb} \mathbf{n}_{ij} A_{ij}^c, \tag{25}$$

⁵ The product, $\|\mathbf{v}_{j,\tau}^c - \mathbf{v}_{i,\tau}^c\| \Delta t$ has dimensions of length.

where $0 \leq K_{ij}^{nb}$ is a bonding constant and p_b is a material parameter.

- If the particles have an activated normal bond, then the particles automatically have a rotational/tangential bond equivalent in form to stick friction

$$\Psi_{ij}^{bond,r} = K_{ij}^{rb} \| \mathbf{v}_{j,\tau}^c - \mathbf{v}_{i,\tau}^c \| A_{ij}^c \Delta t \boldsymbol{\tau}_{ij}^c. \tag{26}$$

We note the choices of the values of the coefficients and exponents are given later in the paper when a numerical example is given.

5 Particle interaction with external forces

5.1 Near-field/electromagnetic forces

Following Zohdi [80], the electromagnetic forces are decomposed into three contributions, (1) Lorentz forces (for charged particles), (2) magnetic forces (for magnetic particles) and (3) inter-particle near-field forces

$$\begin{aligned} \Psi_i^{e+m} &= \Psi_i^{lor,e+m} + \Psi_i^{mag} + \underbrace{\sum_{j \neq i}^N \Psi_{ij}^{nf}}_{\Psi_i^{nf}} \\ &= \underbrace{q_i (\mathbf{E}^{ext} + \mathbf{v}_i \times \mathbf{B}^{ext})}_{\Psi_i^{lor,e+m}} + \Psi_i^{mag} + \Psi_i^{nf}, \end{aligned} \tag{27}$$

where $\sum_{j \neq i}^N \Psi_{ij}^{nf}$ represents the interaction between particle i and all other particles $j = 1, 2 \dots N$ ($j \neq i$), $\Psi_i^{lor,e+m}$ represents external Lorentz-induced forces from the surrounding environment, for example comprised of \mathbf{E}^{ext} and \mathbf{B}^{ext} , which are externally-controlled fields that are independent of the response of the system. The terms \mathbf{E}^{ext} and \mathbf{B}^{ext} can be considered as static (or extremely slowly-varying), and thus mutually uncoupled and independently controllable. The self-induced magnetic fields developed between particles is insignificant (Jackson [38]) for the velocity ranges of interest here (well below the speed of light).

5.1.1 Inter-particle near-field interaction

Following Zohdi [80], a simple form that captures the essential near-field effects is

$$\Psi_i^{nf} = \sum_{j \neq i}^{N_p} \left(\underbrace{\alpha_{1ij} \| \mathbf{r}_i - \mathbf{r}_j \|^{-\beta_1}}_{\text{attraction}} - \underbrace{\alpha_{2ij} \| \mathbf{r}_i - \mathbf{r}_j \|^{-\beta_2}}_{\text{repulsion}} \right) \mathbf{n}_{ij}, \tag{28}$$

where the α 's and β 's are empirical material parameters. The various representations (decompositions) of the coefficients that appear in Eq. 28 are with $c_i = \pm 1$ (a positive/negative identifier): (a) mass-based ($m = \text{mass}$): $\alpha_{ij} = \bar{\alpha}_{ij} m_i m_j c_i c_j$, (b) surface area-based ($a = \text{surface area}$): $\alpha_{ij} = \bar{\alpha}_{ij} a_i a_j c_i c_j$, (c) volume-based ($V = \text{volume}$): $\alpha_{ij} = \bar{\alpha}_{ij} V_i V_j c_i c_j$ and (d) charge-based: $\alpha_{ij} = \bar{\alpha}_{ij} q_i q_j c_i c_j$, where the $\bar{\alpha}_{ij}$ are empirical material parameters. There are vast numbers of empirical representations, for example, found in the field of “molecular dynamics” (MD), which typically refers to mathematical models of systems of atoms or molecules where each atom (or molecule) is represented by a material point and is treated as a point mass. The overall motion of such mass-point systems is dictated by Newtonian mechanics. For an extensive survey of MD-type interaction forces, which includes comparisons of the theoretical and computational properties of a variety of interaction laws, we refer the reader to Frenklach and Carner [31]. In the usual MD approach (see Haile [35], for example), the motion of individual atoms is described by Newton’s second law with the forces computed from differentiating a prescribed potential energy function, with applications to solids, liquids, and gases, as well as biological systems (Hase [36], Schlick [57] and Rapaport [54]). The interaction functions usually take the form of the familiar Mie, Lennard-Jones, and Morse potentials (Moelwyn-Hughes [50]), however three-body terms can be introduced directly into the interaction functions (Stillinger [58]) or, alternatively, “local” modifications can be made to two-body representations (Tersoff [59]).

5.1.2 Magnetic forces

An additional force can be exerted on magnetic particles, independent of the electrodynamically-induced Lorentz forces. A relatively simple model for the characterization of this force is given by

$$\Psi_i^{mag} = \nabla (\gamma \mathbf{B}^{ext} \cdot \mathbf{B}^{ext}), \tag{29}$$

where γ is a material parameter that is related to the magnetization of the particle, and which is dependent on the magnetic dipole properties, the magnetic susceptibility, the magnetic permeability and the internal magnetic moment density of the material (see Feynman et al. [30], Cullity and Graham [20], Boyer [11] or Jackson [38]). For the specific applications in this paper, Ψ_i^{mag} is considered small, relative to the other forces, and can be neglected.

5.2 Interstitial damping

Finally, we note that damping from interstitial fluid (or even smaller-scale particles, solvents) between particles, such as binding enhancers, surfactants and lubricants is possible. A

simple model to account for this is (a very low Reynolds number “Stokesian” model)

$$\Psi_i^{damp} = c^e 6\pi R_i (\mathbf{v}^e - \mathbf{v}_i) \tag{30}$$

where c^e is usually taken to be the fluid viscosity, \mathbf{v}^e is the local average velocity of the external interstitial medium, which one may assume to be $\mathbf{v}^e \approx \mathbf{0}$, for most applications of interest presently. The mechanics of the interstitial fluid is unimportant in problems of interest here, however, for other applications, such as high-speed flow, the motion of the fluid can be important, necessitating more sophisticated drag laws and/or fully coupled (two-way) particle-fluid interaction models. This is outside the scope of the present work. Generally, this requires the use of solid-fluid staggering-type schemes (for example, see Zohdi [74,76] and Avci and Wrighgers [5]).

6 System time-stepping

Integrating Eq. 1 leads to (using a trapezoidal rule with variable integration metric, $0 \leq \phi \leq 1$)

$$\begin{aligned} \mathbf{v}_i(t + \Delta t) &= \mathbf{v}_i(t) + \frac{1}{m_i} \int_t^{t+\Delta t} \Psi_i^{tot} dt \\ &\approx \mathbf{v}_i(t) + \frac{\Delta t}{m_i} (\phi \Psi_i^{tot}(t + \Delta t) + (1 - \phi) \Psi_i^{tot}(t)), \end{aligned} \tag{31}$$

where $\Psi_i^{tot} = \Psi_{ii}^{ray} + \Psi_i^{con} + \Psi_i^{bond} + \Psi_i^{damp} + \Psi_i^{e+m}$. The position can be computed via application of the trapezoidal rule again:

$$\mathbf{r}_i(t + \Delta t) \approx \mathbf{r}_i(t) + \Delta t (\phi \mathbf{v}_i(t + \Delta t) + (1 - \phi) \mathbf{v}_i(t)), \tag{32}$$

which can be consolidated into

$$\begin{aligned} \mathbf{r}_i(t + \Delta t) &= \mathbf{r}_i(t) + \mathbf{v}_i(t) \Delta t \\ &+ \frac{\phi(\Delta t)^2}{m_i} (\phi \Psi_i^{tot}(t + \Delta t) + (1 - \phi) \Psi_i^{tot}(t)). \end{aligned} \tag{33}$$

This leads to a coupled system of equations, which are solved using an adaptive iterative scheme, building on approaches found in various forms in Zohdi [71–80].

6.1 Iterative (implicit) solution method-algorithm

Following the basic framework in Zohdi [80], we write Eq. 33 in a slightly more streamlined form for particle i

$$\begin{aligned} \mathbf{r}_i^{L+1} &= \mathbf{r}_i^L + \mathbf{v}_i^L \Delta t \\ &+ \frac{\phi(\Delta t)^2}{m_i} (\phi(\Psi_i^{tot,L+1}) + (1 - \phi)(\Psi_i^{tot,L})), \end{aligned} \tag{34}$$

which leads to a coupled set equations for $i = 1, 2 \dots N_p$ particles, where the superscript L is a time interval counter. Appendix 3 provides details on this solution process. The solution steps are, within a time-step:

- (0) Determine the ray force contribution for each particle according to the previously explained algorithm (BOX 9)
- (1) Start a global fixed iteration (set $i = 1$ (particle counter) and $K = 0$ (iteration counter))
- (2) If $i > N_p$ then go to (4)
- (3) If $i \leq N_p$ then:
 - (a) Compute the position $\mathbf{r}_i^{L+1,K}$
 - (b) Go to (2) for the next particle ($i = i + 1$)
- (4) Measure error (normalized) quantities
 - (a) $\varpi_K \stackrel{\text{def}}{=} \frac{\sum_{i=1}^{N_p} \|\mathbf{r}_i^{L+1,K} - \mathbf{r}_i^{L+1,K-1}\|}{\sum_{i=1}^{N_p} \|\mathbf{r}_i^{L+1,K} - \mathbf{r}_i^L\|}$
 - (b) $Z_K \stackrel{\text{def}}{=} \frac{\varpi_K}{TOL_r}$
 - (c) $\Lambda_K \stackrel{\text{def}}{=} \left(\frac{(\frac{TOL_r}{\varpi_0})^{\frac{1}{pK_d}}}{(\frac{\varpi_K}{\varpi_0})^{\frac{1}{pK}}} \right)$ (see Appendix 3)
- (5) If the tolerance is met: $Z_K \leq 1$ and $K < K_d$ then
 - (a) Increment time: $t = t + \Delta t$
 - (b) Construct the next time step: $(\Delta t)^{new} = \Lambda_K (\Delta t)^{old}$,
 - (c) Select the minimum size: $\Delta t = \text{MIN}((\Delta t)^{lim}, (\Delta t)^{new})$
 - (d) Update the ray positions and go to (0)
- (6) If the tolerance is not met: $Z_K > 1$ and $K < K_d$ then
 - (a) Update the iteration counter: $K = K + 1$
 - (b) Reset the particle counter: $i = 1$
 - (c) Go to (2)
- (7) If the tolerance is not met ($Z_K > 1$) and $K = K_d$ then
 - (a) Construct a new time step: $(\Delta t)^{new} = \Lambda_K (\Delta t)^{old}$
 - (b) Restart at time t and go to (1)

Time-step size adaptivity is critical, since the system’s dynamics and configuration can dramatically change over the course of time, possibly requiring quite different time step sizes to control the iterative error. However, to maintain the accuracy of the time-stepping scheme, one must respect an upper bound dictated by the discretization error, i.e., $\Delta t \leq \Delta t^{lim}$. Note that in step (5), Λ_K may enlarge the time-step if the error is lower than the preset tolerance.

Remark Although thermal effects were not considered, the algorithm can be modified to account for coupled thermal effects. In those cases, the parameters, such as K_{pij} can be thermally dependent since the particles can thermally soften. For example, the compliance constant for the particles in the contact law can be written as (here Θ is the temperature, which is fixed in the present analysis):

$$K_{pi} = \text{MAX} \left(K_{pio} \left(e^{-a_i \left(\frac{\Theta_i}{\Theta_i^*} - 1 \right)} \right), K_{pi}^{lim} \right), \quad (35)$$

and for particle j

$$K_{pj} = \text{MAX} \left(K_{pjo} \left(e^{-a_j \left(\frac{\Theta_j}{\Theta_j^*} - 1 \right)} \right), K_{pj}^{lim} \right), \quad (36)$$

and take the average at the interface and the value in the contact law:

$$K_{pij} = \frac{1}{2} (K_{pi} + K_{pj}). \quad (37)$$

There is a multitude of possible representations, and it is relatively easy to select one or the other, and to embed in the staggering framework developed. A fully coupled thermal model is not considered here, and we refer the reader to Zohdi [81] for more details in that direction.

7 Numerical example

As an example, we consider a group of N_p randomly dispersed spherical particles, of equal size, generated within in a spherical (aggregate) domain of diameter D . For illustration purposes only (Fig. 6), the radius of the pulse cross-section and the agglomeration radius were both set to unity (one meter). The ratio of particle diameter, d , to total domain diameter, D , was $d/D = 0.05$. The total initial energy (again for illustration purposes) of each pulse was set to $I(t = 0) = I_o = 7.06 \times 10^{13}$ J, which roughly corresponded to a pressure pulse of 150 MPa traveling at a velocity of 1500 m/s over the area of the pulse. The initial energy for each ray was calculated as I/N_r , where $N_r = 10,000$ was the

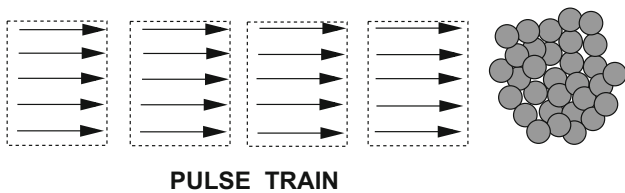


Fig. 6 Pulsing a free-standing agglomeration

number of rays in the beam. We remark that in the example calculation, we used $N_p = 2000$ particles and $N_r = 10,000$ rays, initially parallel arranged in a circular (pulse cross-section) but randomly placed (Fig. 7). This system provided stable results, i.e. increasing the number of rays and/or the number of particles beyond these levels resulted in negligibly different overall system responses. We note successive refinement of the ray density from 1000, 2000, 3000... 10,000 total rays, was found to produce no noticeable differences beyond 10,000 rays. Thus, we can consider, for all practical purposes, that the results are independent of ray-grid density. One can consider the representation of a beam by multiple rays as simply taking a large “sampling” of the diffraction by the beam (wave front) over the portion of the scatterer where the beam is incident, as opposed to a discretization technique. It is relatively simple to scale the geometry down to agglomerations of practical interest, and to use corresponding pulse-energy contents. The ratio of refractive indices was set to $\tilde{c} \stackrel{\text{def}}{=}} \frac{c_i}{c_t} = 1500/4500$, where $c_i = 1500$ m/s (water) and $c_t = 4500$ m/s (ceramic). The densities were set to $\rho_i = 1000$ kg/m³ (water) and $\rho_t = 6000$ kg/m³ (ceramic). This leads to a ratio of acoustical impedances of $\hat{A} = 18$ and, consequently, a reflectivity, at a zero angle of incidence, from Eq. 2, of

$$\mathcal{R}(\theta = 0) = \left(\frac{18 - 1}{18 + 1} \right)^2 = 0.944. \quad (38)$$

Thus, at a zero angle of incidence, the amount of energy transmitted is approximately $1 - 0.944 = 0.056$. In order to generate the random particle positions, the classical random sequential addition (RSA) algorithm was used to place nonoverlapping particles into the domain of interest (Widom [68]), initially a sphere, which was then allowed to dynamically converge to an equilibrium state.⁶ The following relevant other simulation parameters chosen were (in SI-units if not explicitly stated):

- The normal contact parameter was $K_{po} = 10^7$ N/m², at a fixed temperature, $K_p = \text{MAX} \left(K_{po} \left(e^{-a \left(\frac{\Theta}{\Theta^*} - 1 \right)} \right), K_p^{lim} \right)$, where $\Theta^* = 500^\circ$ Kelvin, $K_p^{lim} = 10^6$ N/m², the exponent in the contact law was set to $p_p = 2$, the temperature was fixed to be $\Theta = 300^\circ$ Kelvin and the thermal sensitivity parameter was set to $a = 1$,
- The contact damping parameter, $c^{cd} = 10^5$,
- The friction contact parameter $K^f = 10^7$,
- The coefficient of static friction, $\mu_s = 0.4$,
- The coefficient of dynamic friction, $\mu_d = 0.3$,

⁶ See Torquato [60] and Torquato and coworkers (see, for example, Kansaal et al. [39] and Donev et al. [23–27]) for a detailed review of particle packing algorithms.

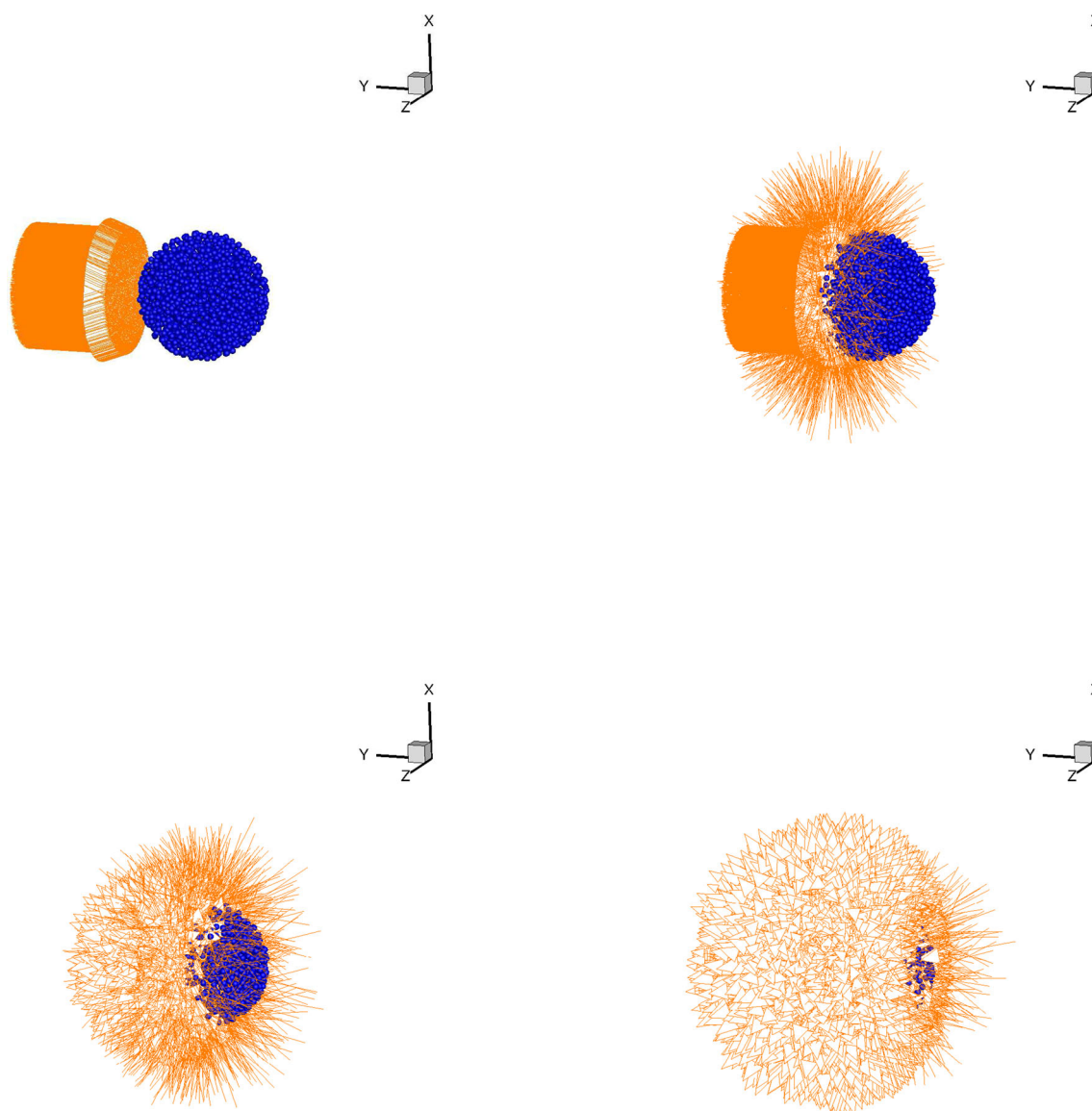


Fig. 7 From left to right and top to bottom, the progressive movement of rays comprising a beam. The vector lengths indicate the energy associated with the ray

- The normal bond parameter, $K^{nb} = 10^6 \text{ N/m}^2$ and the exponent in the binding law was set to $p_b = 2$,
- The rotational/tangential bond parameter, $K^{rb} = 10^3$,
- The interstitial damping coefficient $c^e = 1$ (assumed Stokesian-like),
- The target number of fixed point iterations, $K_d = 10$,
- The trapezoidal time-stepping parameter, $\phi = 0.5$,
- The simulation duration, 2 s,
- The initial time step size, 0.00001 s,
- The time step upper bound, 0.00025 s and
- The tolerance for the fixed-point iteration, 5×10^{-4} .

Figures 7 and 8 illustrate the results after a single pulse. After approximately 4 pulses, for the parameters chosen in this

paper, this agglomeration was completely broken up and dispersed. The number of reflections was 59,238 for this samples problem. Several other statistical realizations were generated with on the order of 58,000–62,000 reflections incurred. Figure 9 shows the accumulated number of reflections after four pulses.

8 Closing statements

In summary, this work developed a discrete-ray/discrete-particle model to characterize the acoustical energy associated with pulses with agglomerations of discrete particles. The approach provides a simpler alternative to a direct

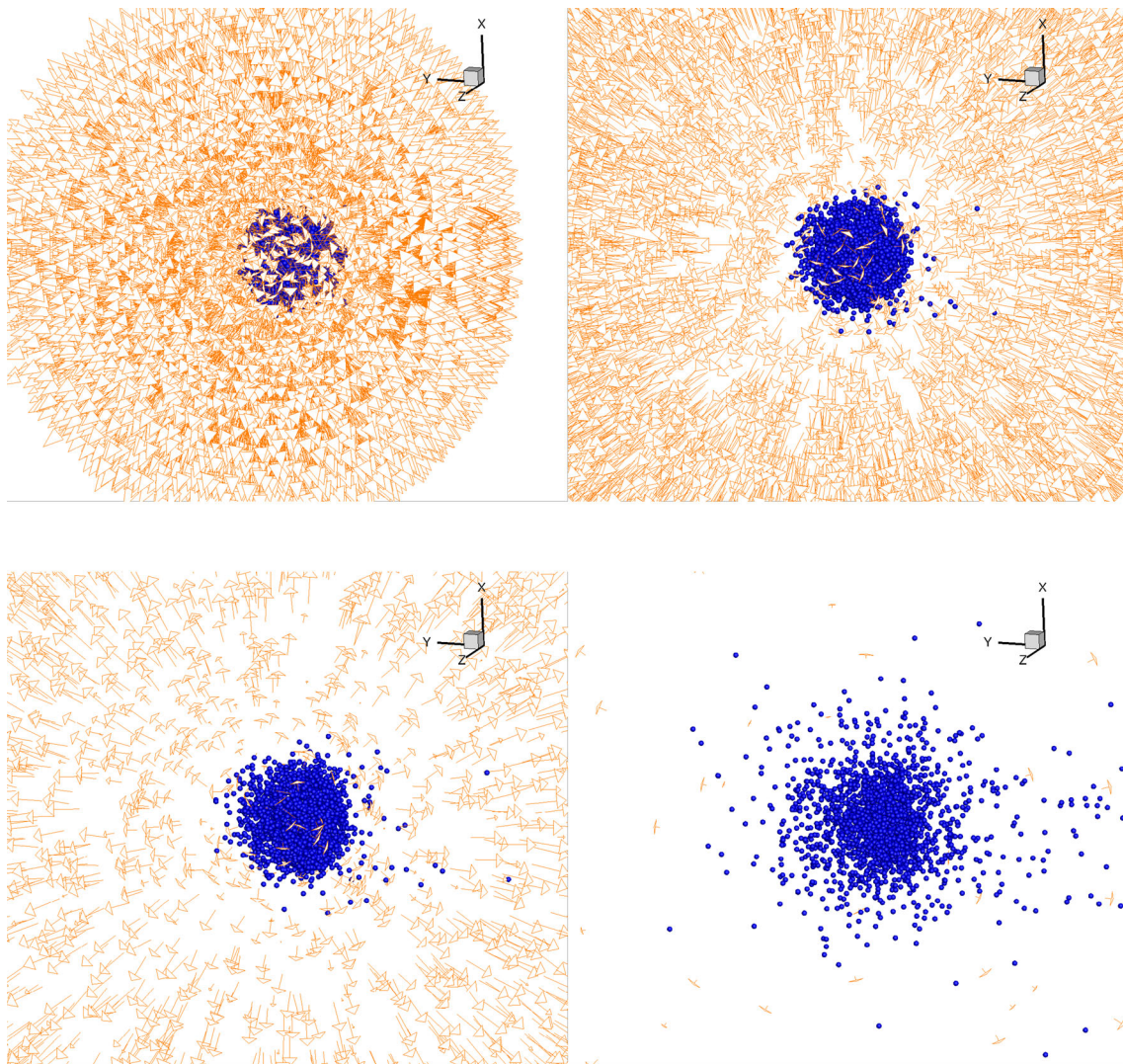


Fig. 8 From left to right and top to bottom, the progressive movement of rays comprising a beam. The vector lengths indicate the energy associated with the ray

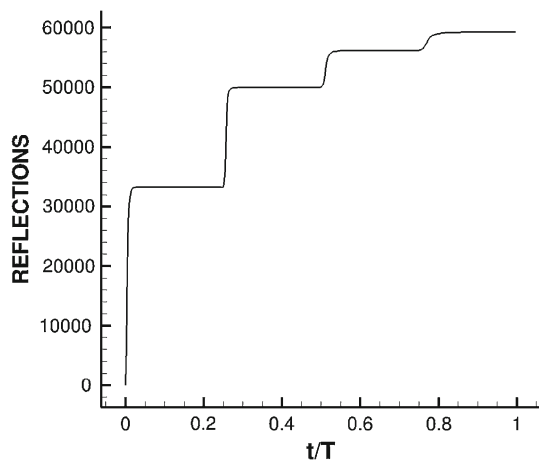


Fig. 9 The number of ray reflections as a function of time for 4 successive pulses

computationally intensive discretization of a continuum description, if it is even possible. Because of the complex microstructure, containing gaps and interfaces, this type of system is extremely difficult to simulate using continuum-based methods, such as the finite difference time domain method or the finite element method. The simplified model captures the primary effects, namely, reflection and absorption of acoustical energy via: (1) a discrete element representation of the particle system (2) a discretization of a concentrated pulse into rays (3) a discrete ray-tracking algorithm is developed to track the propagation of rays and (4) a discrete element method to track the break up and dynamics of the agglomeration. *The simulations take on the order of two minutes on a laptop.* This technique was used to determine the amount of propagating incident energy that was reflected and the amount that was absorbed by each particle. Three

dimensional examples were given to illustrate the method. In closing, there are limitations in the use of ray theory. In particular, for small particles with size on the order of the wavelength, ray theory is inappropriate. Limitations of ray tracing are elaborated upon in Appendix 1.

The paper focused only on the propagation of acoustical energy in the system. The energy that was absorbed was assumed “available” to move the material. Clearly, not all of the absorbed energy would be “converted” into motion, however this serves as a simple conservative estimate of the effects. The purpose of the present work was only to isolate one aspect of the complex series of events associated with shock-type loading of agglomerated microstructures—mainly the determination of the energy absorbed and the system dynamics that would result. The approach developed provides a fast computational tool to analyze particulate agglomerations. It can be used on virtually any type of agglomeration domain. Since the results are derived from a direct numerical simulation, one can also post-process detailed statistical information for the break up metrics. It is relatively straightforward to track quantities of interest related to the rays that comprise the acoustical disturbance, for example, the (normalized) acoustical energy retained in the beam, defined similarly:

$$\begin{aligned} \mathcal{I}_x &\stackrel{\text{def}}{=} \frac{\sum_{q=1}^{N_r} \mathbf{I}_q^{ray} \cdot \mathbf{e}_x}{\sum_{q=1}^{N_r} \|\mathbf{I}_q^{ray}(t=0)\|} \quad \text{and} \\ \mathcal{I}_y &\stackrel{\text{def}}{=} \frac{\sum_{q=1}^{N_r} \mathbf{I}_q^{ray} \cdot \mathbf{e}_y}{\sum_{q=1}^{N_r} \|\mathbf{I}_q^{ray}(t=0)\|} \quad \text{and} \\ \mathcal{I}_z &\stackrel{\text{def}}{=} \frac{\sum_{q=1}^{N_r} \mathbf{I}_q^{ray} \cdot \mathbf{e}_z}{\sum_{q=1}^{N_r} \|\mathbf{I}_q^{ray}(t=0)\|}. \end{aligned} \tag{39}$$

where \mathbf{I}_q^{ray} are the individual ray contributions (Fig. 10). This can be extended, for example, for any quantity of interest, Q (for example the positions of the particles and their velocities), with a distribution of values ($Q_i, i=1, 2, \dots, N_p =$ particles) about an arbitrary reference point, denoted Q^* , as follows:

$$M_r^{Q_i-Q^*} \stackrel{\text{def}}{=} \frac{\sum_{i=1}^{N_p} a_i (Q_i - Q^*)^r}{\sum_{i=1}^{N_p} a_i} \stackrel{\text{def}}{=} \overline{(Q_i - Q^*)^r}. \tag{40}$$

The various moments characterize the distribution, for example:

- (1) $M_1^{Q_i-A}$ measures the first deviation from the average, which equals zero,
- (2) $M_1^{Q_i-0} \stackrel{\text{def}}{=} \frac{\sum_{i=1}^{N_p} a_i (Q_i-0)}{\sum_{i=1}^{N_p} a_i} \stackrel{\text{def}}{=} \overline{(Q_i - 0)} = A,$
- (3) $M_2^{Q_i-A}$ is the standard deviation,

- (4) $M_3^{Q_i-A}$ is the skewness, which measures the bias, or asymmetry of the distribution of data and
- (5) $M_4^{Q_i-A}$ is the kurtosis (fourth moment), which measures the “tightness” of the distribution.

For example, for the purposes of particle dynamics, $a_i = m_i$. This is straightforward to implement, and can provide much more detailed information on post-impact system characteristics.

Appendix 1: Basics of acoustics

In our approach, we model the individual particles as being rigid, and the material surrounding the particles as being isotropic and having a relatively low shear modulus, in the zero limit becoming an acoustical medium. Generally, for an isotropic material, one has the classical relationship between the components of infinitesimal strain (ϵ) to the Cauchy stress (σ)

$$\sigma = \mathbb{E} : \epsilon = 3\kappa \frac{\text{tr}\epsilon}{3} \mathbf{1} + 2\mu \epsilon', \tag{41}$$

where \mathbb{E} is the elasticity tensor and where ϵ' is the strain deviator. The corresponding strain energy density is

$$W = \frac{1}{2} \epsilon : \mathbb{E} : \epsilon = \frac{1}{2} \left(9\kappa \left(\frac{\text{tr}\epsilon}{3} \right)^2 + 2\mu \epsilon' : \epsilon' \right). \tag{42}$$

We focus on the dilatational deformation in the low-shear modulus matrix surrounding the particles. This naturally leads to an idealized “acoustical” material approximation, $\mu \approx 0$. Hence, Eq. 41 collapses to $\sigma = -p\mathbf{1}$, where the pressure is $p = -3\kappa \frac{\text{tr}\epsilon}{3} \mathbf{1}$ and with a corresponding strain energy of $W = \frac{1}{2} \frac{p^2}{\kappa}$. By inserting the simplified expression of the stress $\sigma = -p\mathbf{1}$ into the equation of equilibrium, we obtain

$$\nabla \cdot \sigma = -\nabla p = \rho \ddot{\mathbf{u}}, \tag{43}$$

where \mathbf{u} is the displacement. By taking the divergence of both sides, and recognizing that $\nabla \cdot \mathbf{u} = -\frac{p}{\kappa}$, we obtain

$$\nabla^2 p = \frac{\rho}{\kappa} \ddot{p} = \frac{1}{c^2} \ddot{p}. \tag{44}$$

If we assume a harmonic solution, we obtain

$$\begin{aligned} p &= P e^{j(k \cdot r - \omega t)} \Rightarrow \dot{p} = P j \omega e^{j(k \cdot r - \omega t)} \\ &\Rightarrow \ddot{p} = -P \omega^2 e^{j(k \cdot r - \omega t)}, \end{aligned} \tag{45}$$

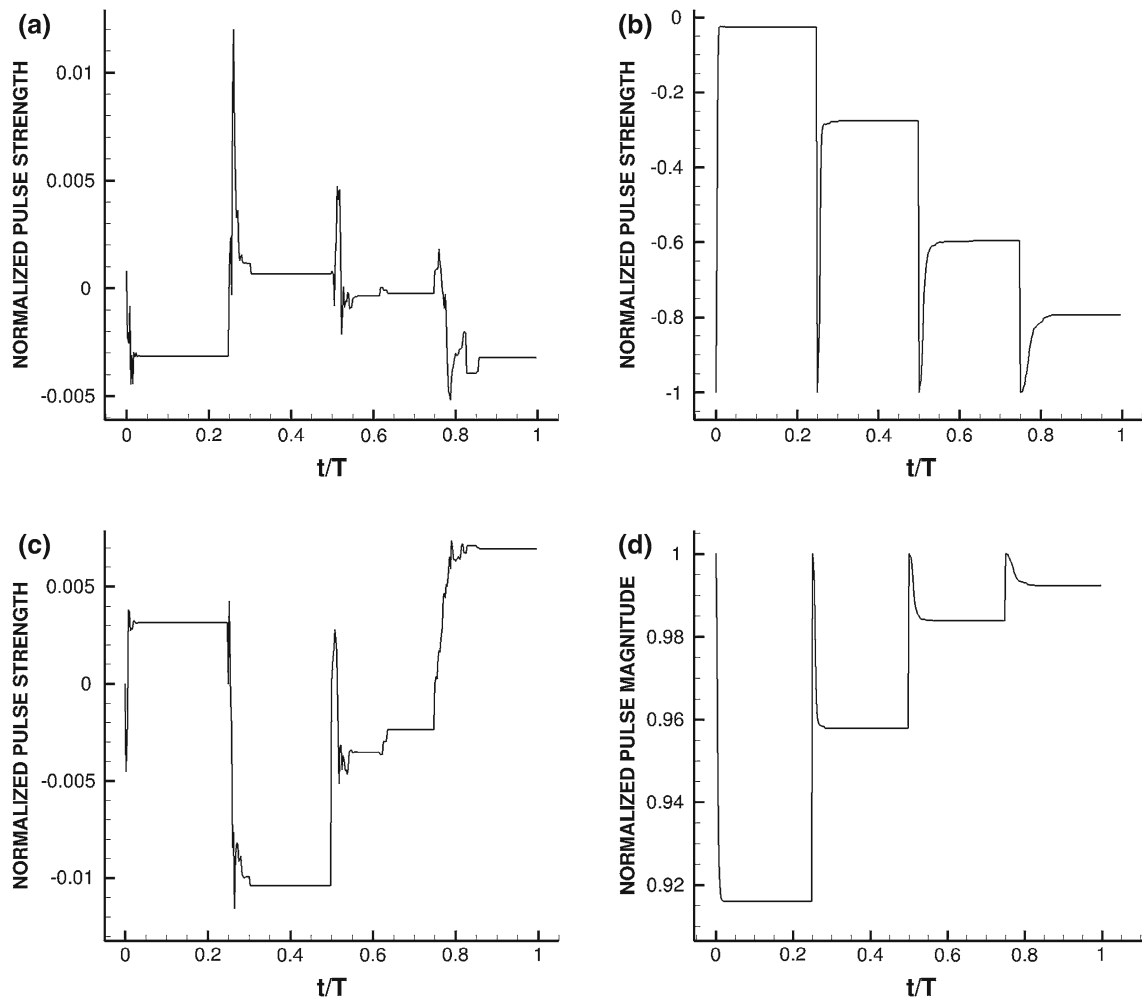


Fig. 10 TOP TO BOTTOM AND LEFT TO RIGHT: **a** Normalized pulse strength in the x-direction: $\mathcal{I}_x \stackrel{\text{def}}{=} \frac{\sum_{q=1}^{N_r} \mathbf{I}_q^{ray} \cdot \mathbf{e}_x}{\sum_{q=1}^{N_r} \|\mathbf{I}_q^{ray}(t=0)\|}$. **b** Normalized pulse strength in the y-direction: $\mathcal{I}_y \stackrel{\text{def}}{=} \frac{\sum_{q=1}^{N_r} \mathbf{I}_q^{ray} \cdot \mathbf{e}_y}{\sum_{q=1}^{N_r} \|\mathbf{I}_q^{ray}(t=0)\|}$. **c** Normalized

pulse strength in the y-direction: $\mathcal{I}_z \stackrel{\text{def}}{=} \frac{\sum_{q=1}^{N_r} \mathbf{I}_q^{ray} \cdot \mathbf{e}_z}{\sum_{q=1}^{N_r} \|\mathbf{I}_q^{ray}(t=0)\|}$. **d** Normalized pulse magnitude: $\frac{\sqrt{\sum_{q=1}^{N_r} ((\mathbf{I}_q^{ray} \cdot \mathbf{e}_x)^2 + (\mathbf{I}_q^{ray} \cdot \mathbf{e}_y)^2 + (\mathbf{I}_q^{ray} \cdot \mathbf{e}_z)^2)}}{\sum_{q=1}^{N_r} \|\mathbf{I}_q^{ray}(t=0)\|}$

and

$$\begin{aligned} \nabla p &= Pj(k_x \mathbf{e}_x + k_y \mathbf{e}_y + k_z \mathbf{e}_z) e^{j(\mathbf{k} \cdot \mathbf{r} - \omega t)} \\ \Rightarrow \nabla \cdot \nabla p &= \nabla^2 p = -P \underbrace{(k_x^2 + k_y^2 + k_z^2)}_{\|\mathbf{k}\|^2} e^{j(\mathbf{k} \cdot \mathbf{r} - \omega t)}. \end{aligned} \tag{46}$$

We insert these relations into Eq. 44, and obtain an expression for the magnitude of the wave number vector

$$-P \|\mathbf{k}\|^2 e^{j(\mathbf{k} \cdot \mathbf{r} - \omega t)} = -\frac{\rho}{\kappa} P \omega^2 e^{j(\mathbf{k} \cdot \mathbf{r} - \omega t)} \Rightarrow \|\mathbf{k}\| = \frac{\omega}{c}. \tag{47}$$

Equation 43 (balance of linear momentum) implies

$$\rho \ddot{\mathbf{u}} = -\nabla p = -Pj(k_x \mathbf{e}_x + k_y \mathbf{e}_y + k_z \mathbf{e}_z) e^{j(\mathbf{k} \cdot \mathbf{r} - \omega t)}. \tag{48}$$

Now we integrate once, which is equivalent to dividing by $-j\omega$, and obtain the velocity

$$\dot{\mathbf{u}} = \frac{Pj}{\rho\omega} (k_x \mathbf{e}_x + k_y \mathbf{e}_y + k_z \mathbf{e}_z) e^{j(\mathbf{k} \cdot \mathbf{r} - \omega t)}, \tag{49}$$

and do so again for the displacement

$$\mathbf{u} = \frac{Pj}{\rho\omega^2} (k_x \mathbf{e}_x + k_y \mathbf{e}_y + k_z \mathbf{e}_z) e^{j(\mathbf{k} \cdot \mathbf{r} - \omega t)}. \tag{50}$$

Thus, we have

$$\|\dot{\mathbf{u}}\| = \frac{P}{c\rho}. \tag{51}$$

The reflection of a plane harmonic pressure wave at an interface is given by enforcing continuity of the (acoustical)

pressure and disturbance velocity at that location; this yields the ratio between the incident and reflected pressures. We use a local coordinate system (Fig. 3), and require that the number of waves per unit length in the x – direction must be the same for the incident, reflected and refracted (transmitted) waves,

$$k_i \cdot e_x = k_r \cdot e_x = k_t \cdot e_x. \tag{52}$$

From the pressure balance at the interface, we have

$$P_i e^{j(k_i \cdot r - \omega t)} + P_r e^{j(k_r \cdot r - \omega t)} = P_t e^{j(k_t \cdot r - \omega t)}, \tag{53}$$

where P_i is the incident pressure ray, P_r is the reflected pressure ray, and P_t is the transmitted pressure ray. This forces a time-invariant relation to hold at all parts on the boundary, because the arguments of the exponential must be the same. This leads to ($k_i = k_r$)

$$k_i \sin \theta_i = k_r \sin \theta_r \Rightarrow \theta_i = \theta_r, \tag{54}$$

and

$$k_i \sin \theta_i = k_t \sin \theta_t \Rightarrow \frac{k_i}{k_t} = \frac{\sin \theta_t}{\sin \theta_i} = \frac{\omega/c_t}{\omega/c_i} = \frac{c_i}{c_t} = \frac{v_i}{v_t} = \frac{n_t}{n_i}. \tag{55}$$

Equations 52 and 53 imply

$$P_i e^{j(k_i \cdot r)} + P_r e^{j(k_r \cdot r)} = P_t e^{j(k_t \cdot r)}. \tag{56}$$

The continuity of the displacement, and hence the velocity

$$v_i + v_r = v_t, \tag{57}$$

leads to, after use of Eq. 51,

$$-\frac{P_i}{\rho_i c_i} \cos \theta_i + \frac{P_r}{\rho_r c_r} \cos \theta_r = -\frac{P_t}{\rho_t c_t} \cos \theta_t. \tag{58}$$

We solve for the ratio of the reflected and incident pressures to obtain

$$r = \frac{P_r}{P_i} = \frac{\hat{A} \cos \theta_i - \cos \theta_t}{\hat{A} \cos \theta_i + \cos \theta_t}, \tag{59}$$

where $\hat{A} \stackrel{\text{def}}{=} \frac{A_t}{A_i} = \frac{\rho_t c_t}{\rho_i c_i}$, where ρ_t is the medium which the ray encounters (transmitted), c_t is corresponding sound speed in that medium, A_t is the corresponding acoustical impedance, ρ_i is the medium in which the ray was traveling (incident), c_i is corresponding sound speed in that medium A_i is the corresponding acoustical impedance. The relationship (the

law of refraction) between the incident and transmitted angles is $c_t \sin \theta_t = c_i \sin \theta_i$. Thus, we may write the Fresnel relation

$$r = \frac{\tilde{c} \hat{A} \cos \theta_i - (\tilde{c}^2 - \sin^2 \theta_i)^{\frac{1}{2}}}{\tilde{c} \hat{A} \cos \theta_i + (\tilde{c}^2 - \sin^2 \theta_i)^{\frac{1}{2}}}, \tag{60}$$

where $\tilde{c} \stackrel{\text{def}}{=} \frac{c_i}{c_t}$. The reflectance for the (acoustical) energy $\mathcal{R} = r^2$ is

$$\mathcal{R} = \left(\frac{P_r}{P_i}\right)^2 = \left(\frac{\hat{A} \cos \theta_i - \cos \theta_t}{\hat{A} \cos \theta_i + \cos \theta_t}\right)^2 = \left(\frac{I_r}{I_i}\right)^2. \tag{61}$$

For the cases where $\sin \theta_t = \frac{\sin \theta_i}{\tilde{c}} > 1$, one may rewrite the reflection relation as

$$r = \frac{\tilde{c} \hat{A} \cos \theta_i - j(\sin^2 \theta_i - \tilde{c}^2)^{\frac{1}{2}}}{\tilde{c} \hat{A} \cos \theta_i + j(\sin^2 \theta_i - \tilde{c}^2)^{\frac{1}{2}}}. \tag{62}$$

where $j = \sqrt{-1}$. The reflectance is $\mathcal{R} \stackrel{\text{def}}{=} r \bar{r} = 1$, where \bar{r} is the complex conjugate. Thus, for angles above the critical angle $\theta_i \geq \theta_i^*$, all of the energy is reflected. We note that when $A_t = A_i$ and $c_i = c_t$, then there is no reflection. Also, when $A_t \gg A_i$ or when $A_t \ll A_i$, then $r \rightarrow 1$.

Remark If one considers for a moment an incoming pressure wave (ray), which is incident on an interface between two general elastic media ($\mu \neq 0$), reflected shear waves must be generated in order to satisfy continuity of the traction, $\|\sigma \cdot n\| = 0$ This is due to the fact that

$$\| (3\kappa \text{tr} \frac{\epsilon}{3} \mathbf{1} + 2\mu \epsilon') \cdot n \| = 0. \tag{63}$$

For an idealized acoustical medium, $\mu = 0$, no shear waves need to be generated to satisfy Eq. 63.

Appendix 2: Contact area parameter and alternative models

Contact area parameter

Following Zohdi [80], and referring to Fig. 11, one can solve for an approximation of the common contact radius a_{ij} (and the contact area, $A_{ij}^c = \pi a_{ij}^2$) by solving the following three equations,

$$a_{ij}^2 + L_i^2 = R_i^2, \tag{64}$$

and

$$a_{ij}^2 + L_j^2 = R_j^2, \tag{65}$$

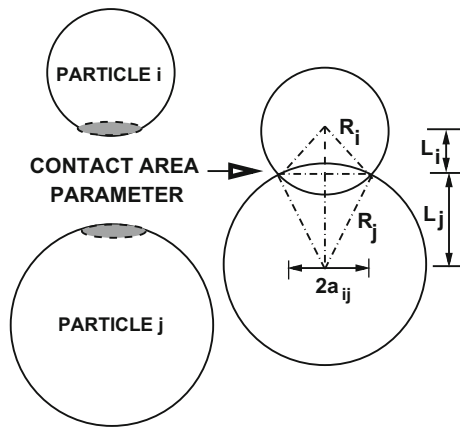


Fig. 11 An approximation of the contact area parameter for two particles in contact (see Zohdi [80])

and

$$L_i + L_j = \|\mathbf{r}_i - \mathbf{r}_j\|, \tag{66}$$

where R_i is the radius of particle i , R_j is the radius of particle j , L_i is the distance from the center of particle i and the common contact interpenetration line and L_j is the distance from the center of particle j and the common contact interpenetration line, where the extent of interpenetration is

$$\delta_{ij} = R_i + R_j - \|\mathbf{r}_i - \mathbf{r}_j\|. \tag{67}$$

The above equations yield an expression a_{ij} , which yields an expression for the contact area parameter

$$A_{ij}^c = \pi a_{ij}^2 = \pi(R_i^2 - L_i^2), \tag{68}$$

where

$$L_i = \frac{1}{2} \left(\|\mathbf{r}_i - \mathbf{r}_j\| - \frac{R_j^2 - R_i^2}{\|\mathbf{r}_i - \mathbf{r}_j\|} \right). \tag{69}$$

Alternative models

One could easily construct more elaborate relations connecting the relative proximity of the particles and other metrics to the contact force, $\Psi_{ij}^{con,n} \propto \mathcal{F}(\mathbf{r}_i, \mathbf{r}_j, \mathbf{n}_{ij}, R_i, R_j, \dots)$, building on, for example, Hertzian contact models. This poses no difficulty in the direct numerical method developed. For the remainder of the analysis, we shall use the deformation metric in Eq. 14. For detailed treatments, see Wellman et al. [63–67] and Avci and Wriggers [5]. We note that with the appropriate definition of parameters, one can recover Hertz, Bradley, Johnson–Kendell–Roberts, Derjaguin–Muller–Toporov contact models. For example, Hertzian contact is widely used, with the assumptions being

- frictionless, continuous, surfaces,
- each of contacting bodies are elastic half-spaces, whereby the contact area dimensions are smaller radii of the bodies and,
- the bodies remain elastic (infinitesimal strains),

results in the following contact force:

$$\Psi_{ij}^{con,n} = \frac{4}{3} (R^*)^{1/2} E^* \delta_{ij}^{3/2} \mathbf{n}_{ij}, \tag{70}$$

which has the general form of $\Psi^{con,n} = K_{ij}^* \delta_{ij}^p$, where

- $R^* = \left(\frac{1}{R_i} + \frac{1}{R_j} \right)^{-1}$ and
- $E^* = \left(\frac{1-\nu_i^2}{E_i} + \frac{1-\nu_j^2}{E_j} \right)^{-1}$,

where E is the Young’s modulus and ν is the Poisson ratio, The contact area with such a model has already been incorporated in the relation above, and is equal to $A_{ij}^c = \pi a^2$ where $a = \sqrt{R^* \delta_{ij}}$. For more details, we refer the reader to Johnson [40]. It is obvious that for a deeper understanding of the deformation within a particle, it must be treated as a deformable continuum, which would require a highly-resolved spatial discretization, for example using the Finite Element Method for the contacting bodies. This requires a large computational effort. For the state of the art in finite element methods and contact mechanics, see the books of Wriggers [69,70]. For work specifically focusing on the continuum mechanics of particles, see Zohdi and Wriggers [75].

Appendix 3: Iterative solution method

The set of equations represented by Eq. 34 can be solved recursively. Equation 34 can be solved recursively by recasting the relation as

$$\begin{aligned} \mathbf{r}_i^{L+1,K} &= \mathbf{r}_i^L + \mathbf{v}_i^L \Delta t + \frac{(\phi \Delta t)^2}{m_i} \Psi_i^{tot,L+1,K-1} \\ &\quad + \frac{\phi(\Delta t)^2}{m_i} (1 - \phi) \Psi_i^{tot,L}, \end{aligned} \tag{71}$$

which is of the form

$$\mathbf{r}_i^{L+1,K} = \mathcal{G}(\mathbf{r}_i^{L+1,K-1}) + \mathcal{L}_i, \tag{72}$$

where $K = 1, 2, 3, \dots$ is the index of iteration within time step $L + 1$ and

$$\Psi_i^{tot,L+1,K-1} \stackrel{\text{def}}{=} \left(\mathbf{r}_1^{L+1,K-1}, \mathbf{r}_2^{L+1,K-1} \dots \mathbf{r}_N^{L+1,K-1} \right), \Psi_i^{tot,L+1,K-1}$$

- $\Psi_i^{tot,L} \stackrel{\text{def}}{=} \Psi_i^{tot,L}(\mathbf{r}_1^L, \mathbf{r}_2^L \dots \mathbf{r}_N^L)$,
- $\mathcal{G}(\mathbf{r}_i^{L+1,K-1}) = \frac{(\phi \Delta t)^2}{m_i} \Psi_i^{tot,L+1,K-1}$ and
- $\mathcal{L}_i = \mathbf{r}_i^L + \mathbf{v}_i^L \Delta t + \frac{\phi(\Delta t)^2}{m_i} (1 - \phi) \Psi_i^{tot,L}$.

The term \mathcal{L}_i is a remainder term that does not depend on the solution. The convergence of such a scheme is dependent on the behavior of \mathcal{G} . Namely, a sufficient condition for convergence is that \mathcal{G} is a contraction mapping for all $\mathbf{r}_i^{L+1,K}$, $K = 1, 2, 3 \dots$. In order to investigate this further, we define the iteration error as

$$\varpi_i^{L+1,K} \stackrel{\text{def}}{=} \mathbf{r}_i^{L+1,K} - \mathbf{r}_i^{L+1} \tag{73}$$

A necessary restriction for convergence is iterative self consistency, i.e. the “exact” (discretized) solution must be represented by the scheme, $\mathbf{r}_i^{L+1} = \mathcal{G}(\mathbf{r}_i^{L+1}) + \mathcal{L}_i$. Enforcing this restriction, a sufficient condition for convergence is the existence of a contraction mapping

$$\begin{aligned} \underbrace{\|\mathbf{r}_i^{L+1,K} - \mathbf{r}_i^{L+1}\|}_{\varpi_i^{L+1,K}} &= \|\mathcal{G}(\mathbf{r}_i^{L+1,K-1}) - \mathcal{G}(\mathbf{r}_i^{L+1})\| \\ &\leq \eta^{L+1,K} \|\mathbf{r}_i^{L+1,K-1} - \mathbf{r}_i^{L+1}\|, \end{aligned} \tag{74}$$

where, if $0 \leq \eta^{L+1,K} < 1$ for each iteration K , then $\varpi_i^{L+1,K} \rightarrow \mathbf{0}$ for any arbitrary starting value $\mathbf{r}_i^{L+1,K=0}$, as $K \rightarrow \infty$, which is a contraction condition that is sufficient, but not necessary, for convergence. The convergence of Eq. 71 is scaled by $\eta \propto \frac{(\phi \Delta t)^2}{m_i}$. Therefore, we see that the contraction constant of \mathcal{G} is:

- directly dependent on the magnitude of the interaction forces ($\|\Psi\|$),
- inversely proportional to the masses m_i and
- directly proportional to $(\Delta t)^2$.

Thus, decreasing the time step size improves the convergence. *In order to maximize the time-step sizes (to decrease overall computing time) and still meet an error tolerance on the numerical solution’s accuracy*, we build on an approach originally developed for continuum thermo-chemical multifield problems (Zohdi [71]), where one assumes: (1) $\eta^{L+1,K} \approx S(\Delta t)^p$, (S is a constant) and (2) the error within an iteration behaves according to $(S(\Delta t)^p)^K \varpi^{L+1,0} = \varpi^{L+1,K}$, $K = 1, 2, \dots$, where $\varpi^{L+1,0} = \mathbf{r}^{L+1,K=1} - \mathbf{r}^L$ is the initial norm of the iterative (relative) error and S is intrinsic to the system. For example, for second-order problems, due to the quadratic dependency on Δt , $p \approx 2$. The objective is to meet an error tolerance in exactly a preset (the analyst sets this) number of iterations. To this end, one writes $(S(\Delta t_{\text{tol}})^p)^{K_d} \varpi^{L+1,0} = TOL$, where TOL is a tolerance and where K_d is the number of desired iterations. If the error

tolerance is not met in the desired number of iterations, the contraction constant $\eta^{L+1,K}$ is too large. Accordingly, one can solve for a new smaller step size, under the assumption that S is constant,

$$\Delta t_{\text{tol}} = \Delta t \left(\frac{(\frac{TOL}{\varpi^{L+1,0}})^{\frac{1}{pK_d}}}{(\frac{\varpi^{L+1,K}}{\varpi^{L+1,0}})^{\frac{1}{pK}}} \right) \stackrel{\text{def}}{=} \Delta t \Lambda_K \tag{75}$$

The assumption that S is constant is not critical, since the time steps are to be recursively refined and unrefined throughout the simulation. Clearly, the expression in Eq. 75 can also be used for time step enlargement, if convergence is met in less than K_d iterations (typically chosen to be between five to ten iterations).

References

1. Afazov SM, Becker AA, Hyde TH (2012) Mathematical modeling and implementation of residual stress mapping from microscale to macroscale finite element models. *J Manuf Sci Eng* 134(2):021001-021001-11
2. Arbelaez D, Zohdi TI, Dornfeld D (2008) Modeling and simulation of material removal with particulate flow. *Comput Mech* 42:749–759
3. Arbelaez D, Zohdi TI, Dornfeld D (2009) On impinging near-field granular jets. *Int J Numer Methods Eng* 80(6):815–845
4. Aurich JC, Dornfeld DA (2010) In: JC Aurich, DA Dornfeld (eds) *Proceedings of the CIRP international on burrs: analysis, control and removal*. Springer, Berlin
5. Avci B, Wriggers P (2012) A DEM-FEM coupling approach for the direct numerical simulation of 3D particulate flows. *J Appl Mech* 79:010901-1–010901-7
6. Avila M, Gardner J, Reich-Weiser C, Tripathi Vijayaraghavan A, Dornfeld DA (2005) Strategies for burr minimization and cleanability in aerospace and automotive manufacturing. *SAE Technical Paper* 2005-01-3327. doi:10.4271/2005-01-3327
7. Avila M, Reich-Weiser C, Dornfeld DA, McMains S (2006) Design and manufacturing for cleanability in high performance cutting. *CIRP 2nd international conference on high performance cutting*, paper number 63. Vancouver
8. Bagherifard S, Giglio M, Giudici L, Guagliano M (2010) Experimental and numerical analysis of fatigue properties improvement in a titanium alloy by shot peening. In: *Proceedings of the ASME*. 49163, ASME 2010 10th biennial conference on engineering systems design and analysis, vol 2, pp 317–322
9. Bolintineanu DS, Grest GS, Lechman JB, Pierce F, Plimpton SJ, Schunk PR (2014) Particle dynamics modeling methods for colloidal suspensions. *Comput Part Mech* 1(3):321–356
10. Borejko P, Chen CF, Pao YH (2011) Application of the method of generalized rays to acoustic waves in a liquid wedge over elastic bottom. *J Comput Acoust* 9(01):41–68
11. Boyer Timothy H (1988) The force on a magnetic dipole. *Am J Phys* 56(8):688–692. doi:10.1119/1.15501 Bibcode:1988AmJPh.56.688B
12. Cante J, Davalos C, Hernandez JA, Oliver J, Jonsen P, Gustafsson G, Haggblad HA (2014) PFEM-based modeling of industrial granular flows. *Comput Part Mech* 1(1):47–70
13. Carbonell JM, Onate E, Suarez B (2010) Modeling of ground excavation with the particle finite element method. *J Eng Mech ASCE* 136:455–463

14. Chen Z, Yang F, Meguid SA (2014) Realistic finite element simulations of arc-height development in shot-peened Almen strips. *J Eng Mater Technol* 136(4):041002–041002-7
15. Choi S, Park I, Hao Z, Holman HY, Pisano AP, Zohdi TI (2010) Ultra-fast self-assembly of micro-scale particles by open channel flow. *Langmuir* 26(7):4661–4667
16. Choi S, Stassi S, Pisano AP, Zohdi TI (2010) Coffee-ring effect-based three dimensional patterning of micro, nanoparticle assembly with a single droplet. *Langmuir* 26(14):11690–11698
17. Choi S, Jamshidi A, Seok TJ, Zohdi TI, Wu MC, Pisano AP (2012) Fast, high-throughput creation of size-tunable micro, nanoparticle clusters via evaporative self-assembly in picoliter-scale droplets of particle suspension. *Langmuir* 28(6):3102–3111
18. Ciampini D, Spelt JK, Papini M (2003) Simulation of interference effects in particle streams following impact with a flat surface. Part I. Theory and analysis. *Wear* 254:237–249
19. Ciampini D, Spelt JK, Papini M (2003) Simulation of interference effects in particle streams following impact with a flat surface. Part II. Parametric study and implications for erosion testing and blast cleaning. *Wear* 254:250–264
20. Cullity BD, Graham CD (2008) Introduction to magnetic materials (2 ed). Wiley-IEEE Press, p 103. ISBN 0-471-47741-9
21. Demko M, Choi S, Zohdi TI, Pisano AP (2012) High resolution patterning of nanoparticles by evaporative self-assembly enabled by in-situ creation and mechanical lift-off of a polymer template. *Appl Phys Lett* 99:253102-1–253102-3
22. Demko MT, Cheng JC, Pisano AP (2010) High-resolution direct patterning of gold nanoparticles by the microfluidic molding process. *Langmuir*, pp 412–417
23. Donev A, Cisse I, Sachs D, Variano EA, Stillinger F, Connelly R, Torquato S, Chaikin P (2004a) Improving the density of jammed disordered packings using ellipsoids. *Science* 303:990–993
24. Donev A, Stillinger FH, Chaikin PM, Torquato S (2004b) Unusually dense crystal ellipsoid packings. *Phys Rev Lett* 92:255506
25. Donev A, Torquato S, Stillinger F (2005a) Neighbor list collision-driven molecular dynamics simulation for nonspherical hard particles-I. Algorithmic details. *J Comput Phys* 202:737
26. Donev A, Torquato S, Stillinger F (2005b) Neighbor list collision-driven molecular dynamics simulation for nonspherical hard particles-II. Application to ellipses and ellipsoids. *J Comput Phys* 202:765
27. Donev A, Torquato S, Stillinger FH (2005c) Pair correlation function characteristics of nearly jammed disordered and ordered hard-sphere packings. *Phys Rev E* 71:011105
28. Duran J (1997) Sands, powders and grains. An introduction to the physics of granular matter. Springer, Berlin
29. Elbella A, Fadul F, Uddanda SH, Kasarla NR (2012) Influence of shot peening parameters on process effectiveness. In: Proceedings of the ASME, 45196, vol 3: design, materials and manufacturing, parts A, B, and C, pp 2015–2021
30. Feynman RP, Leighton RB, Sands M (2006) The Feynman Lectures on Physics 2. ISBN 0-8053-9045-6
31. Frenklach M, Carmer CS (1999) Molecular dynamics using combined quantum & empirical forces: application to surface reactions. *Adv Class Traject Methods* 4:27–63
32. Gomes-Ferreira C, Ciampini D, Papini M (2004) The effect of interparticle collisions in erosive streams on the distribution of energy flux incident to a flat surface. *Tribol Int* 37:791–807
33. Ghoheity A, Spelt JK, Papini M (2008) Abrasive jet micro-machining of planar areas and transitional slopes. *J Micromech Microeng* 18:055014
34. Ghoheity A, Krajac T, Burzynski T, Papini M, Spelt JK (2008) Surface evolution models in abrasive jet micromachining. *Wear* 264:185–198
35. Haile JM (1992) Molecular dynamics simulations: elementary methods. Wiley, New York
36. Hase WL (1999) Molecular dynamics of clusters, surfaces, liquids, & interfaces. Advances in classical trajectory methods, vol 4. JAI Press, Greenwich
37. Garg S, Dornfeld D, Berger K (2010) Formulation of the chip cleanability mechanics from fluid transport. In: Aurich JC, Dornfeld DA (eds) Burrs analysis, control and removal. Springer, Berlin, pp 229–236
38. Jackson JD (1998) Classical electrodynamics, 3rd edn. Wiley, New York
39. Kansaal A, Torquato S, Stillinger F (2002) Diversity of order and densities in jammed hard-particle packings. *Phys Rev E* 66:041109
40. Johnson K (1985) Contact mechanics. Cambridge University Press, Cambridge
41. Luo L, Dornfeld DA (2001) Material removal mechanism in chemical mechanical polishing: theory and modeling. *IEEE Trans Semicond Manuf* 14(2):112–133
42. Luo L, Dornfeld DA (2003) Effects of abrasive size distribution in chemical-mechanical planarization: modeling and verification. *IEEE Trans Semicond Manuf* 16:469–476
43. Luo L, Dornfeld DA (2003) Material removal regions in chemical mechanical planarization for sub-micron integration for sub-micron integrated circuit fabrication: coupling effects of slurry chemicals, abrasive size distribution, and wafer-pad contact area. *IEEE Trans Semicond Manuf* 16:45–56
44. Luo L, Dornfeld DA (2004) Integrated modeling of chemical mechanical planarization of sub-micron IC fabrication. Springer, Berlin
45. Labra C, Onate E (2009) High-density sphere packing for discrete element method simulations. *Commun Numer Methods Eng* 25(7):837–849
46. Leonardi A, Wittel FK, Mendoza M, Herrmann HJ (2014) Coupled DEM-LBM method for the free-surface simulation of heterogeneous suspensions. *Comput Part Mech* 1(1):3–13
47. Markauskasa D, Maknickas A, Kacianauskas R (2015) Simulation of acoustic particle agglomeration in poly-dispersed aerosols. *Proced Eng* 102:1218–1225
48. Martin P (2009) Handbook of deposition technologies for films and coatings, 3rd edn. Elsevier, Oxford
49. Martin P (2011) Introduction to surface engineering and functionally engineered materials. Scrivener and Elsevier. *J Vac Sci Technol A* 2(2):500
50. Moelwyn-Hughes EA (1961) Physical chemistry. Pergamon, London
51. Onate E, Idelsohn SR, Celigueta MA, Rossi R (2008) Advances in the particle finite element method for the analysis of fluid-multibody interaction and bed erosion in free surface flows. *Comput Methods Appl Mech Eng* 197(19–20):1777–1800
52. Onate E, Celigueta MA, Idelsohn SR, Salazar F, Surez B (2011) Possibilities of the particle finite element method for fluid-soil-structure interaction problems. *Comput Mech* 48:307–318
53. Onate E, Celigueta MA, Latorre S, Casas G, Rossi R, Rojek J (2014) Lagrangian analysis of multiscale particulate flows with the particle finite element method. *Comput Part Mech* 1(1):85–102
54. Rapaport DC (1995) The art of molecular dynamics simulation. Cambridge University Press, Cambridge
55. Rojek J, Labra C, Su O, Onate E (2012) Comparative study of different discrete element models and evaluation of equivalent micromechanical parameters. *Int J Solids Struct* 49:1497–1517. doi:10.1016/j.ijsolstr.2012.02.032
56. Rojek J (2014) Discrete element thermomechanical modelling of rock cutting with valuation of tool wear. *Comput Part Mech* 1(1):71–84
57. Schlick T (2000) Molecular modeling & simulation. An interdisciplinary guide. Springer, New York
58. Stillinger FH, Weber TA (1985) Computer simulation of local order in condensed phases of silicon. *Phys Rev B* 31:5262–5271

59. Tersoff J (1988) Empirical interatomic potential for carbon, with applications to amorphous carbon. *Phys Rev Lett* 61:2879–2882
60. Torquato S (2002) Random heterogeneous materials: microstructure & macroscopic properties. Springer, New York
61. Virovlyanskii AL (1995) Interrelation between ray and mode field representations in an acoustic waveguide. *Radiophys Quant Electron* 38:76
62. Wei C, Dong J (2014) Development and modeling of melt electrohydrodynamic-jet printing of phase-change inks for high-resolution additive manufacturing. *J Manuf Sci Eng* 136:061010. doi:[10.1115/1.4028483](https://doi.org/10.1115/1.4028483) Paper No: MANU-14-1179
63. Wellmann C, Lillie C, Wriggers P (2008) A contact detection algorithm for superellipsoids based on the common-normal concept. *Eng Comput* 25:432–442
64. Wellmann C, Lillie C, Wriggers P (2008) Homogenization of granular material modelled by a three-dimensional discrete element method. *Comput Geotech* 35:394–405
65. Wellmann C, Lillie C, Wriggers P (2008) Comparison of the macroscopic behavior of granular materials modeled by different constitutive equations on the microscale. *Finite Elem Anal Des* 44:259–271
66. Wellmann C, Wriggers P (2011) In: Onate E, Owen DRJ (eds) Homogenization of granular material modeled by a 3D DEM, particle-based methods: fundamentals and applications, pp. 211–231
67. Wellmann C, Wriggers P (2012) A two-scale model of granular materials. *Comput Methods Appl Mech Eng* 205–208:46–58
68. Widom B (1966) Random sequential addition of hard spheres to a volume. *J Chem Phys* 44:3888–3894
69. Wriggers P (2002) Computational contact mechanics. Wiley, New York
70. Wriggers P (2008) Nonlinear finite element analysis. Springer, Berlin
71. Zohdi TI (2002) An adaptive-recursive staggering strategy for simulating multifield coupled processes in microheterogeneous solids. *Int J Numer Methods Eng* 53:1511–1532
72. Zohdi TI (2003) On the compaction of cohesive hyperelastic granules at finite strains. *Proc R Soc* 454(2034):1395–1401
73. Zohdi TI (2007) P-wave induced energy and damage distribution in agglomerated granules. *Model Simul Mater Sci Eng* 15:S435–S448
74. Zohdi TI (2007) Computation of strongly coupled multifield interaction in particle-fluid systems. *Comput Methods Appl Mech Eng* 196:3927–3950
75. Zohdi TI, Wriggers P (2008) Introduction to computational micro-mechanics. Second Reprinting. Springer, Berlin
76. Zohdi TI (2014) Embedded electromagnetically sensitive particle motion in functionalized fluids. *Comput Part Mech* 1:27–45
77. Zohdi TI (2012) Estimation of electrical-heating load-shares for sintering of powder mixtures. *Proc R Soc* 468:2174–2190
78. Zohdi TI (2012) Dynamics of charged particulate systems. Modeling, theory and computation. Springer, Berlin
79. Zohdi TI (2013) Numerical simulation of charged particulate cluster-droplet impact on electrified surfaces. *J Comput Phys* 233:509–526
80. Zohdi TI (2014) A direct particle-based computational framework for electrically-enhanced thermo-mechanical sintering of powdered materials. *Math Mech Solids*, pp 1–21. doi:[10.1007/s11831-013-9092-6](https://doi.org/10.1007/s11831-013-9092-6)
81. Zohdi TI (2014) Additive particle deposition and selective laser processing—a computational manufacturing framework. *Comput Mech* 54:171–191
82. Zohdi TI (2015) On the thermal response of a laser-irradiated powder particle in additive manufacturing. *CIRP J Manuf Sci Technol*. doi:[10.1016/j.cirpj.2015.05.001](https://doi.org/10.1016/j.cirpj.2015.05.001)
83. Zohdi TI (2015) Modeling and simulation of the post-impact trajectories of particles in oblique precision shot-peening. *Comput Part Mech*. doi:[10.1007/s40571-015-0048-5](https://doi.org/10.1007/s40571-015-0048-5)
84. Zohdi TI (2006) On the optical thickness of disordered particulate media. *Mech Mater* 38:969–981
85. Zohdi TI, Kuypers FA (2006) Modeling and rapid simulation of multiple red blood cell light scattering. *Proc R Soc Interface* 3(11):823–831
86. Zohdi TI (2006) Computation of the coupled thermo-optical scattering properties of random particulate systems. *Comput Methods Appl Mech Eng* 195:5813–5830
87. Zohdi TI (2012) Modeling and simulation of the optical response of rod-functionalized reflective surfaces. *Comput Mech* 50(2):257–268
88. Zohdi TI (2013) Rapid simulation of laser processing of discrete particulate materials. *Arch Comput Methods Eng* 20:309–325
89. Zohdi TI (2015) A computational modelling framework for high-frequency particulate obscurant cloud performance. *Int J Eng Sci* 89:75–85